Lidargrammetric co-matching and co-adjustment – a new method of photogrammetric and LiDAR data integration

Antoni Rzonca [1], Mariusz Twardowski [2]

[1] Faculty of Geo-Data Science, Geodesy, and Environ. Eng., AGH University of Krakow, Poland - arz@agh.edu.pl
[2] Faculty of Geo-Data Science, Geodesy, and Environ. Eng., AGH University of Krakow, Poland - misiekt@agh.edu.pl

Commission I

Keywords: LiDAR, Bundle adjustment, Image matching, Data registration, Lidargrammetry.

Abstract

The accuracy of spatial raw data is contingent on a number of factors, including the accuracy of the sensors, their calibration, and direct and indirect referencing. The efficacy of the captured data can be enhanced through the implementation of effective data processing methodologies. The present research is dedicated to the enhancement of combined photogrammetric and LiDAR data.
In the contemporary context, the trajectory of the vehicle can be affected by GPS signal jamming, a phenomenon that is attributable to international circumstances. This necessitates a combined adjustment of RGB/CIR and LiDAR data. The proposed method necessitates the utilisation of both sets of data: The study area was imaged using both RGB and CIR technologies, with intensity LiDAR strips also employed to cover the same area. The present approach is founded upon the notion of lidargrammetry (Jayendra-Lakshman and Devarajan, 2013), which uses photogrammetric algorithms for lidar data processing (Rzonca and Twardowski, 2022).
The research tool, PyLiGram, generates synthetic images of the LiDAR data, known as lidargrams or renders, applying the same interior orientation parameters (IOPs) as the real camera used to capture the real RGB/CIR images. The synthetic images are centrally projected according to IOPs and predefined external orientation parameters (EOPs). The projection process is reversible by use of unique lidar point identifiers. Points can be projected onto synthetic images, and after processing the same images, points can be intersected to create a new point cloud.
The paper sets out the potential of applying photogrammetric methods to the co-adjustment of RGB/CIR and LiDAR data. The process entails the collaborative processing of RGB/CIR and LiDAR images through the utilisation of deep learning matching techniques and common least squares adjustment. The refined EOPs are then utilised to intersect the refined point cloud and enhance the images' positions.
A key benefit of this approach is that it has the potential to eliminate the necessity for LiDAR control patches/points or ground control points for RGB/CIR images, depending on the specific case.
The process was subjected to a series of trials on multiple datasets, each comprising a point cloud density of approximately 100 points per square metre and images with a ground sample distance (GSD) ranging from 5 to 10 centimetres.

1. Introduction

Lidar data accuracy depends on precision of the scanner and trajectory measurement errors. Further processing allows to enhance the quality of the data. Our research is dedicated to lidar data of low accuracy of the trajectory or without trajectory, for instance even archival data in strips or blocks. Nowadays it occurs that trajectory is affected by GPS signal disruptions caused by international situation. The only demand of the method is to be able to use RGB or CIR images covering the same area. Our approach uses idea of lidar and image data integration for lidar accuracy enhancement. It is based on idea of lidargrammetry which uses photogrammetric algorithms for lidar data processing. Our research tool PyLiGram generates synthetic images of the point cloud, so-named lidargrams. It uses central projection and interior orientation parameters (IOPs) of the real camera used for capturing visual images.
The paper presents the results of our research of application photogrammetric methods for enhancement of lidar data using lidargrammetric approach. Visual images and synthetic images are processed together in one common least-square adjustment. The adjusted external orientation parameters (EOPs) are used to intersect transformed point cloud and, optionally, to enhance the image positions.
The novelty of our approach is elimination of need of any LiDAR control and non-rigid, 3D transformation of the point cloud. Lidargrammetry with specific LiDAR and image point identification is applied as well.
In the first chapter the state of the art is presented: lidar data adjustment methods, data integration for lidar enhancement and contemporary matching pipelines. In the second chapter the method is described, procedure of testing is presented and results of processing of two datasets. In the third chapter the results are discussed and the method will be assessed. Final chapter presents the conclusions and potential of the results in scope of the future research.

2. State of the art

2.1 LiDAR data accuracy

LiDAR data processing has specific steps: registration or adjustment, classification, mapping product generation or automatic objects recognition. The complete review of the method of processing methods of laser scanning is published by Lohani and Ghosh (Lohani and Ghosh, 2017).
In our research the most important part is LiDAR data adjustment named also registration. It is implemented in several software solutions and it is used in mass mapping production for more than two decades (Baltsavias, 1999). The most popular applications adjust the trajectory as a source data using altimetric correction: TerraMatch (Terrasolid Ltd., 2022) and RiProcess (RIEGL Laser Measurement Systems GmbH, 2022).

The horizontal position of the LiDAR strip in defined by GPS and IMU data. The adjustment of the strips relies on altimetric rigid translation and rotations or non-rigid height correction. The horizontal position is unchanged. It is known that practically XYZ control is not applied There are other tools for LiDAR data processing like a research tool OPALS (Pfeifer et al., 2014). In context of our research the most interesting solutions process the LiDAR date without trajectory. The problem was discussed before (Ressl et al., 2009). Usually, these methods are created for research like LiDAR strip adjustment using piecewise tricubic polynomial transformation for railways (Glira et al., 2023).

The development of the technology is parallel with accuracy investigations of the method. Firstly, strips were compared in several ways. One of them was a calculation of the distance between two interpolated DEMs from overlapping strips (Ressl et al., 2008). Next step of such a quality assessment was a 5-parameter transformation of each strip to minimize discrepancies between neighbour strips (Ressl et al., 2009). More advanced method was described in (Habib et al., 2010). Several conjugate elements are applied to relative adjustment of the LiDAR strips like: conjugate points and pseudo conjugate points, areal and linear features, and point-patch pairs. These features can be extracted and matched automatically, and applied for quality assessment of the data.

Application of Unmanned Aerial Vehicles (UAVs) for scanning is possible thanks to light scanners. The problem of their accuracy is widely discussed. One of evaluation and enhancement method is dynamic calibration of the system (Tulldahl et al., 2015). The method allows to get accuracy below 5cm thanks specific correction of the data of low-cost equipment. Mayr et al. present study of UAV LiDAR accuracy for surface deformation in mountain areas basing on multitemporal measurements (Mayr et al., 2020). Dreier et al. evaluate the direct referencing on the UAV LiDAR data using ground control and study of all the accuracy factors that should be taken into account for such a data acquisition (Dreier et al., 2021).

Contemporary studies still focus on the LiDAR accuracy and its potential enhancement. Brun et al. present the method which is based on dynamic network for trajectory adjustment with point-to-point correspondences and raw inertial and GNSS observations (Brun et al., 2022). The effectiveness of the method was proved by adjustment of LiDAR strips with sections without GNSS data. Elaksher et al. describe quantitative analysis of LiDAR data accuracy in height and in plan (Elaksher et al., 2023). Two basic components of different frequency are discussed and their changes are fitted by splines. The precision and accuracy assessment can be presented using automatic detection of chessboards, circular panels and, sets of circular panels (Flood et al., 2024). The presence of the problem of LiDAR accuracy in the research works indicates that LiDAR data accuracy is not able to be completely assessed and its dependence of GNSS signal makes it more unstable than photogrammetric data.

2.2 Data integration for lidar enhancement

In paper of Pirotti et al. accuracy of high density photogrammetric and LiDAR point cloud is compared (Pirotti et al., 2022). The comparison and possibilities to integrate make these two technologies parallel and able to enhance their quality each other. One of the well-known and widely discussed problem of photos and LiDAR data is their co-registration (Kumar Mishra, 2012; Rzonca, 2018). Nowadays most of producers offer the integrated platform for image and LiDAR data acquisition. Leica Geosystems introduces CityMapper 3 (Leica, 2024), Riegl Laser Measurement Systems offers several solutions, the last one platform VQ-1560III-S (Riegl, 2024), and Vexcel Imaging presented Dragon 4.1 (Vexcel, 2024). Each of them is equipped in one or two scanners and RGB and IR one or more cameras. The integrated data can be used for calibration (Pentek et al., 2020) or further processing like DTM generation (Mandlburger et al., 2017) and its evaluation (Zahs et al., 2022). But the most popular application of the integration of both methods is to orientate externally or registrate one of both kinds of data of normal airborne sensors (Toschi et al., 2021; Zhu et al., 2021) or UAV (Bobkowska et al., 2017; Li et al., 2019; Yang and Chen, 2015).

Most of research approaches is based on comparison of the point cloud of dense image matching and LiDAR. We applied an opposite way. We generate photogrammetry-kind data from LiDAR and we match them with RGB or CIR images.

2.3 Matching methods

Development of image matching methods defined completely new possibilities of photogrammetry (Morelli et al., 2022; Zhang et al., 2024). It eliminated stereoscopic measurements with some exceptions and extended image matching possibilities on different images, not only RGB. It has two stages: feature detection and feature matching. There are two main groups of methods of image matching: traditional methods named as hand-crafted methods (like SIFT or SURF) and deep learning methods.

The first important stage of hand-crafted methods development was Harris operator for corner and line features detection using second difference of image (Harris and Stephens, 1988). Scale-invariant feature transform (SIFT) is a standard matching method using Difference of Gaussians to detect the keypoints (Lowe, 2004). Relatively, the process is not fast, so it cannot be applied for real-time matching. The faster but less accurate method is SURF (Speeded Up Robust Features). It is also like SIFT invariant of scale, rotation and photometry and not able to be used for real-time computation. There is also another group of methods applicable to real-time processes: ORB and AKAZE. ORB (Oriented FAST and Rotated BRIEF) is less accurate as SIFT and SURF, but it detect much more features and matches (Rublee et al., 2011). AKAZE is another matching method, less robust, less stable than ORB and also efficient. The above composition is based on review paper of Zhang X. et al. (Zhang et al., 2024). Another method, RIFT (Radiation-Variation Insensitive Feature Transform) does not use the colour, intensity or gradient values for feature detection. It uses phase congruency and it has higher stability in feature detection (Li et al., 2020).

Deep learning methods are second group of methods opening new possibilities to process also images of different kind of sensors. Such a matching is difficult or impossible by hand-crafted methods. The deep learning methods can be divided in two groups: (1) separated feature description and detection process and (2) integrated these processes within one pipeline [31]. Within separated processes several detectors based on CNN were presented: MatchNet (Han et al., 2015), TFeat (Balntas et al., 2016b), L2Net (Tian et al., 2017), HardNet (Mishchuk et al., 2017), PN-Net (Balntas et al., 2016a), SuperPoint (Detone et al., 2018), Key.Net (Barroso Laguna et al., 2019), ALIKE (Zhao et al., 2023b), ALIKED (Zhao et al., 2023a). The matching process has to be done after detection of features like SuperGlue (Sarlin et al., 2020). The nowadays tendence is to join detection and matching in one pipeline (Yoon and Park, 2024). In our research we used Deep Image Learning (DIM) developed by Bruno Kessler Foundation in Trento, Italy (Morelli et al., 2024). DIM is a framework of

several pipelines (SuperPoint + SuperGlue; Superpoint + LightGlue etc.) and integrated processes as end-to-end learning methods like LoFTR (Sun et al., 2021) and RoMa (Edstedt et al., 2023). Another integrated method should be mentioned to present the all state-of-the-art of deep learning matching: DeDoDe (Han et al., 2024).

2.4 Lidargrammetry

Lidargrammetry is a method analogical to photogrammetry. In lidargrammetry one measures so-called lidargrams (or renders): synthetic images of centrally projected point cloud. These images can be processed using photogrammetric methods in four general areas: platform calibration, orientation/registration, stereo observation (Rodríguez-Cielos et al., 2017; Rzonca and Majek, 2016) and measurement and features extraction.
Lidargrammetry applications include its use for extraction of spatial data (Fragkos and Ioannidis, 2016), measuring infrared point data in three dimensions (Teo et al., 2010), and data orientation (Jayendra-Lakshman and Devarajan, 2013). Current research uses synthetic images to achieve deep learning goals, particularly with regard to detection and segmentation (Xianjia et al., 2022).

3. Materials and methods

The core of the method is the use of lidargrammetry and the deep learning matching of RGB images and lidargrams to improve the accuracy of the absolute orientation of one or both of the two integrated data sets: photographs or LiDAR point cloud. There are three basic use cases for this method, which are described in the following subsections.
This approach is pivotal in ensuring the geometrical homogeneity of all the set of data. The ensuing discourse pertains to the precision of the process and the elements that contribute to its efficacy.

3.1 General overview of tested methods

3.1.1 Case 1: LiDAR data refinement

The initial case under consideration pertains to the absence or substandard quality of LiDAR data trajectory (see Figure 1). The block of photogrammetric images (PHOTOS) is adjusted using ground control points (GCPs) and a priori direct referencing data. The block of photos (PHOTOS) has been correctly and finally adjusted. As an input data set for the core of the method – co-matching and co-adjustment, as well as the images and their adjusted external orientation (EO'(PH)) – is matched with lidargrams with external orientation, generated by the PyLiGram tool – research lidargrammetric tool being developed by the authors. L_GRAMs, EO(LG). In conclusion, it is evident that the novel point cloud LiDAR is calculated by means of the PyLiGram tool.

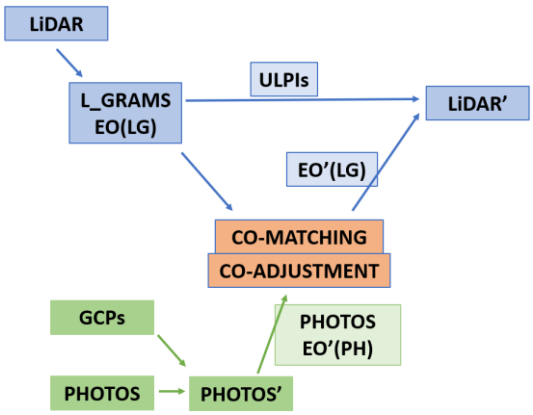

Figure 1. Block scheme of Case 1: LiDAR data refinement

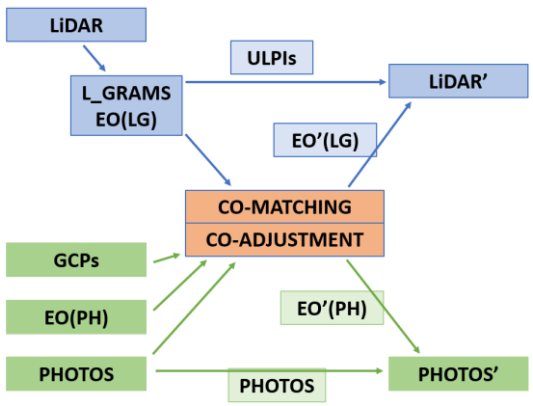

Figure 2. Block scheme of Case 2: Photos and LiDAR data refinement

3.1.2 Case 2: Photos and LiDAR data refinement

The second case is illustrated in Figure 2. Photos, in conjunction with their unadjusted EO(PH) and GCPs, are employed directly in the matching and adjustment process with L_GRAMS and their a priori EO(LG). The LiDAR calculations are performed in the same manner as previously outlined. Furthermore, the external orientation (EO'(PH)) of the adjusted block of RGB images (PHOTOS) is modified.

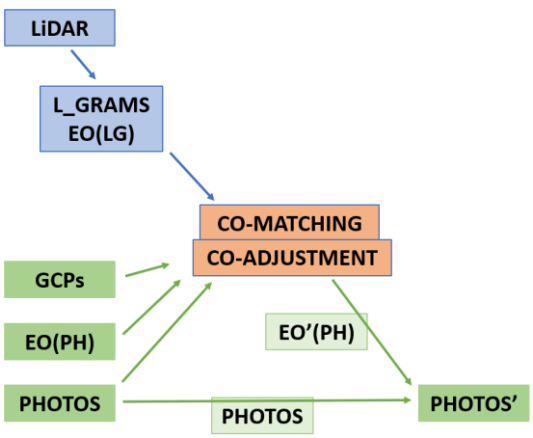

Figure 3. Block scheme of Case 3: Photogrammetric data refinement

3.1.3 Case 3: Photogrammetric data refinement

The third case represents a simplified version of the second case, as illustrated in Figure 3. The LiDAR data is subject to a priori refinement. The outcome of the process of matching and adjusting L_GRAMS and PHOTOS is the adjustment of the RGB block: calculation of EO'(PH).

3.2 Test data

Two sets of data were utilised to evaluate the efficacy of the methodologies, exhibiting variation in terms of land use type, recording platform type, camera resolution, scanner type, ground sample distance (GSD), and point cloud density. In one instance, the block was found to be intact, while in the other, a single row was observed.

3.2.1 Graz test field

The initial test field encompasses the city centre of Graz (Austria). The data has been sourced from the Vexcel Dragon 4.1 system (Vexcel, 2024), comprising nadir photos captured using a fixed 81 mm camera with a resolution of 10560 x 14144 px, in conjunction with a point cloud derived from a 5-line scanner. The test block incorporates a combined point cloud derived from three strips: three merged scan strips and 30 photos that collectively span the same area.
The point cloud contains 112 million points, with an average density of approximately 60 points per square metre, thus yielding an average distance between points of approximately 13 centimetres.
The mean GSD of the photographs is approximately 5 cm.
Consequently, the ratio of GSD to average point distance is 1:2.5.
The utilisation of the PyLiGram research tool resulted in the generation of 30 lidargrams, characterised by identical IOPs to the RGB photos, and analogous EOPs. The RGB photos were converted to black and white images.
The analysis of the three alignment cases was undertaken using ground control points and check points, which were derived from direct GPS measurements and photogrammetric measurements on a reference block. This densification of the control system enabled the establishment of an adequate number and appropriate distribution of control and check points (ChPs), a prerequisite for ensuring the reliability of the results obtained from the verification of the calculations. In conclusion, a total of 20 points were utilised, of which 7 were GCPs and 13 were ChPs.

3.2.2 Loosdorf test field

The second test field is situated in the rural area adjacent to the village of Loosdorf in Austria. The data set under consideration consists of a single strip of images and a point cloud, the capture of which was undertaken using the Riegl VQ-1560 III-S system (Riegl, 2024). It is important to note that for the purposes of the tests, it was only the point cloud obtained from the second red channel that was used, with a density of approximately 16 points/m2, i.e. an average point distance of approximately 25 cm. The same area was covered by 18 photographs with a GSD of approximately 8 cm, obtained with a camera having a focal length of 35.962 mm and a frame size of 8750 x 11664 px.
The ratio of GSD to the mean distance between points is 1:3.
During the preparatory stage, 19 lidargrams were generated with IOPs analogous to those found in an RGB camera image, and EOPs enabling this area to be covered with lidargrams.
For the purposes of this study, the control group was comprised exclusively of points measured on a perfectly aligned strip of photos. The total number of subjects included in the study was 23, of which 4 were used as GCPs and 19 as ChPs.

3.3 Method's testing

Prior to the testing of each of the three variants for both test fields, a number of preparatory steps were taken.

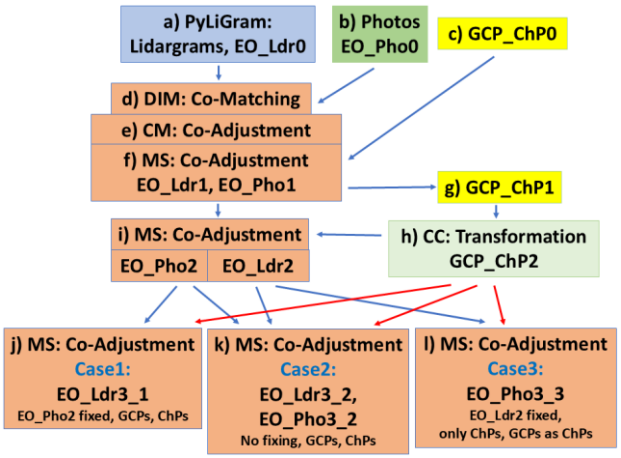

Figure 4. Methods' testing workflow

Figure 4 presents a schematic representation of the workflow for the testing of all three cases. The input data comprised lidargrams and their approximate EOPs (EO_Ldr0) (see Figure 4a), photographs with approximate EOPs (EO_Pho0) (see Figure 4b), and control point coordinates (GCP_ChP0) (see Figure 4c).
The initial phase of the study involved the alignment and preliminary simultaneous alignment of photographs and lidargrams. The matching process was executed through the utilisation of machine learning algorithms, employing a Superpoint model (Detone et al., 2018) for keypoints detection and a Lightglue matcher (Morelli et al., 2024) within the Deep Image Matching software framework, which was developed by the Bruno Kessler Foundation in Trento, Italy (see Figure 4d). The fundamental parameters were set to a low level of quality, with a geometric verification threshold of 1 and a keypoints limit of 10,000. The remaining settings were found to be in their default configuration.
As demonstrated in Figure 5, an example of a mixed pair from the Graz test field is provided, consisting of a photograph and a lidargram. Figure 6 presents the results of their matching, which in this case amounts to approximately 4,000 matches. For the tested Superpoint and Superglue methods, as well as for the medium quality setting, the matching result did not allow for further use due to the low number of matches.

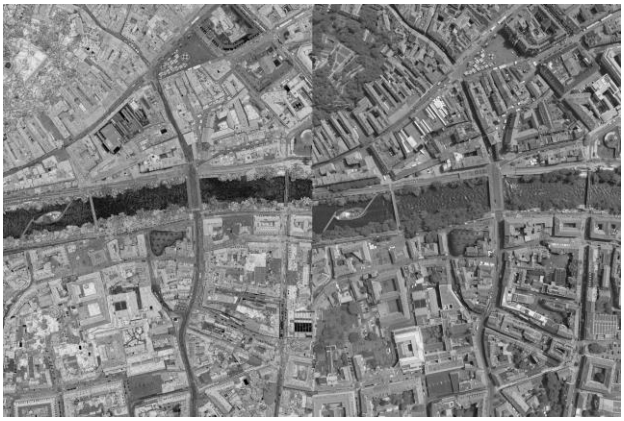

Figure 5. Example images to match: lidargram on the left and photo on the right.

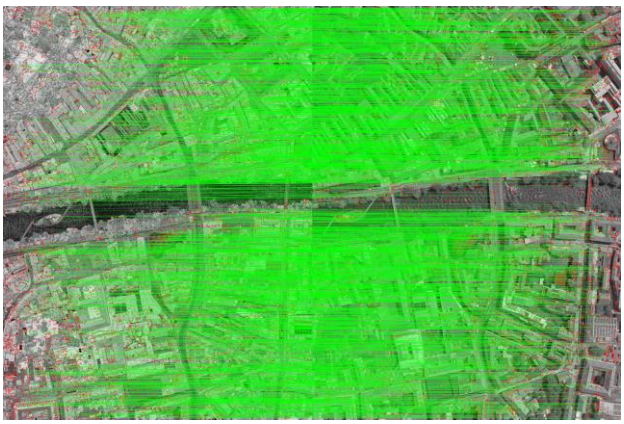

Figure 6. The above images with shown matches

In the subsequent stage of the analysis, the model of all the photographs and their matches was imported into COLMAP software (https://colmap.github.io/, 2025) and subjected to strict alignment (see Figure 4e). The initial evaluation determined the alignment to be correct, on the premise that all images were incorporated within the model.

Subsequently, a project was created in Agisoft Metashape (www.agisoft.com, 2024) (Figure 4f), and the photos and lidargrams, coordinates of GCPs and CHPs, and approximate EOPs for all images were imported. The GCPs and CHPs were measured on the photos, while no measurements were made on the lidargrams due to the potentially low accuracy of observations resulting from the limited visual quality of these synthetic images. A standard camera was designated for the photographic documentation, with its input optical parameters fixed to ensure they remained constant during the adjustment process. The DIM (Morelli et al., 2024) and COLMAP software results, in the form of tie points, were imported into the Metashape project. Following precise alignment in Metashape, the coordinates of the GCPs (GCP_ChP1) (Figure 4g) were exported and, using Cloud Compare software (cloudcompare.org, 2025), a 6-element transformation to the secondary GCP_ChP2 (Figure 4h) system was performed. This resulted in a new set of coordinates to which the test data for each of the three test cases were to be adjusted. The co-adjustment (Figure 4i) was performed, and the EOPs of the photos (EO_Pho2) and lidargrams (EO_Ldr2) were exported in the secondary system.

Subsequently, three copies of the Metashape project were created in the original layout. Each of these copies was then subjected to the following steps, in order to differentiate them according to one of the three cases.

3.3.1 Case 1 testing

Case 1 involved the adjustment of a data set for the external orientation of lidargrams (see Figure 4j). A copy of the Metashape project in the primary alignment (see Figure 4f) was completed with the alignment to the secondary coordinate system EO_Pho2 and GCP_ChP2 coordinates. In this instance, minor EO_Pho2 errors were predetermined, precluding their modification during the alignment process. GCPs served as the reference point. The resultant alignment was subsequently utilised to calculate new EOPs (EO_Ldr3_1), which can be employed for multiple forward intersections of a new point cloud according to the scheme illustrated in Figure 1 (LIDAR'). This is facilitated by the process of lidargram generation, wherein all points that are projected onto the lidargrams are assigned unified LiDAR point identifiers (ULPIs). It is therefore possible to determine, during the inverse process of projecting points onto the lidargram planes, which specific points of the transformed cloud are to be intersected. This determination is made based on the points projected onto the lidargram.

3.3.2 Case 2 testing

Case 2 involves the simultaneous alignment of the EOPs of the lidargrams (EO_Ldr3_2) and of the photos (EO_Pho3_2) (Figure 4k), without blocking with small EO errors any calculated EOPs (Figure 4k). This is therefore a universal case. GCPs were also used as a reference. The resultant outcomes were the adjusted EOPs of lidargrams (EO_Ldr3_2) and of photos (EO_Pho3_2). The utilisation of EOPs of lidargrams (EO_Ldr3_2) facilitates the generation of a novel point cloud through the identification of points with ULPIs.

3.3.3 Case 3 testing

Case 3 results in the adjustment of the EOPs images (EO_Pho3_3) without the use of GCPs (Figure 4l). In this particular instance, all matrix points function as checkpoints. Errors in the EOPs of lidargrams (EO_Ldr2) are set a priori, thereby ensuring their invariance during adjustment. The calculated EOPs of photos (EO_Pho3_3) are accurate due to the tie points to the lidargrams. Therefore, it can be stated in basic terms that this case represents an intermediate orientation of a set of images to a point cloud (represented by lidargrams), with the control for this block of photos being determined by the tie points.

3.3.4 Evaluation method of tests results

The parameters employed for the evaluation of the calculations' precision (along with the proposed methodologies) encompassed the errors on the GCPs and ChPs (in meters), in addition to the reprojection errors in the pixels of the photographs. A comparison of the results of Case 2 with those of Case 1 and Case 3 was undertaken in order to assess whether the two sets of data were sufficiently linked. Furthermore, it was determined whether deep learning matching allowed for alignment at a similar level of accuracy for these two data sets (photos and lidargrams), and indirectly for the point cloud.

4. Results and discussion

4.1 Graz test field

4.1.1 Case 1

The GSD of the photos taken at the Graz test field is 5 cm. The results of the study are summarised in Table 1. The Root Mean Square Error (RMSE) values obtained on the Global Positioning System (GPS) points are approximately 1-1.5 times the reprojection error (RE) of the height, which is about 2.5 times the RE. It is considered that the alignment has been performed correctly when the RE is less than half an image pixel. In such cases, the results (EO_Ldr3_1) can be used to recalculate the transformed point cloud.

	RMSE X [m]	RMSE Y [m]	RMSE Z [m]	RE [px]
GCPs (7)	0.079	0.059	0.126	0.459
ChPs (13)	0.031	0.040	0.113	0.335

Table 1. Case 1: RMSE and reprojection errors of GCPs and ChPs

This is achieved through the utilisation of the ULPIs allocated to the points (along with their respective projections) during the process of generating the lidargrams within the PyLiGram software framework.

4.1.2 Case 2

The second case constitutes the general case in which EOPs of lidargrams (EO_Ldr2) and photos (EO_Pho2) are aligned. It can be concluded that the greater flexibility of the block, as evidenced in this instance, has a significant impact on the accuracy of the results obtained (see Table 2).
At the output, the obtained EOPs of lidargrams (EO_Ldr3) and photos (EO_Pho3) are exemplary, and their reliability is at a similar level despite the different values of GSD of the images and the average distance of the cloud points from which the lidargrams were generated.
.

	RMSE X [m]	RMSE Y [m]	RMSE Z [m]	RE [px]
GCPs (7)	0.077	0.051	0.084	0.448
ChPs (13)	0.012	0.028	0.111	0.335

Table 2. Case 2: RMSE and reprojection errors of GCPs and ChPs

4.1.3 Case 3

The results of this case are given in Table 3. The block of images is aligned exclusively on the basis of its association with the lidargram block. It is evident that no GCPs are utilised in this context; the horizontal RMSE errors obtained on the ChPs demonstrate a high degree of similarity to the RMSE obtained on the GCPs in case 2. In terms of vertical results, the outcomes are twice as unfavourable as in the other cases. The reprojection error is at an appropriate level, falling below half of a pixel.
It is evident that the utilisation of oriented and aligned lidar data (i.e. lidargram blocks) facilitates the orientation of photogrammetric images, thereby ensuring the production of accurate results.

	RMSE X [m]	RMSE Y [m]	RMSE Z [m]	RE [px]
GCPs (0)	-	-	-	-
ChPs (20)	0.077	0.043	0.211	0.375

Table 3. Case 3: RMSE and reprojection errors of ChPs

4.1.4 Comparison

A comparison of the results obtained from the three cases for the Graz test field demonstrates the feasibility of aligning the data correctly in each variant, contingent on the initial data available. In terms of RMSE (both absolute and relative to GSD and cloud density), the results are satisfactory, while a reprojection error of less than 0.5 px confirms the correctness of the observations and adjustment.

4.2 Loosdorf test field

4.2.1 Case 1

The analysis of the results for the Loosdorf test field was carried out in a similar manner. In the former case, the RMSE X and Z errors values for the GCPs and ChPs, as well as an RMSE Y value that was 1.5 times smaller for the control points, were obtained. The RMSE X values were approximately 0.5 GSD, the RMSE Y values were below 2 GSD for GCP and almost slightly above 1 GSD for ChPs, while the RMSE Z was approximately below 1 GSD for both types of reference points. Furthermore, the reprojection error values were found to be very low.

	RMSE X [m]	RMSE Y [m]	RMSE Z [m]	RE [px]
GCPs (4)	0.044	0.138	0.074	0.131
ChPs (19)	0.044	0.090	0.070	0.229

Table 4. Case 1: RMSE and reprojection errors of GCPs and ChPs

4.2.2 Case 2

The second case, in which reference points were selected with a high degree of precision, demonstrated a notably high level of accuracy. While the results are indeed very good, it is imperative to treat them as an approximation, given that they are subject to a priori selected errors, thereby allowing considerable flexibility of the block.

	RMSE X [m]	RMSE Y [m]	RMSE Z [m]	RE [px]
GCPs (4)	0.001	0.002	0.005	0.131
ChPs (19)	0.002	0.002	0.005	0.229

Table 5. Case 2: RMSE and reprojection errors of GCPs and ChPs

4.2.3 Case 3

The alignment of images with lidar data demonstrates minimal RMSE errors, with approximately ¼ GSD of RMSE X and RMSE Y, and less than ½ GSD of RMSE Z. The REs are comparable to those observed in the other two cases.

	RMSE X [m]	RMSE Y [m]	RMSE Z [m]	RE [px]
GCPs (0)	-	-	-	-
ChPs (23)	0.022	0.022	0.033	0.219

Table 6. Case 3: RMSE and reprojection errors of ChPs

4.2.4 Comparison

In this test field, the optimal outcomes were achieved for reference case 2. However, it is noteworthy that for case 3, the RMSE errors are twofold smaller than those obtained for case 1. The presence of reprojection errors that are similar or identical serves to confirm the accuracy of the measurement and alignment processes.

5. Conclusions

The research presented here constitutes a further step in a wider research project on the possibilities of improving the quality of data captured with hybrid sensors. The utilisation of a methodology for the projection of LiDAR data onto virtual image planes, in conjunction with the application of unique identifiers to cloud points (ULPIs) and their images on lidarograms, facilitates the precise reconstruction of the point cloud through the implementation of photogrammetric techniques.

The research phase that has been presented concerns new possibilities for the integration of photogrammetric and lidar data through efficient matching methods based on deep machine learning. The integration of photogrammetry and lidar data facilitates the standardisation of adjustments to the block.

The results presented herein demonstrate that, irrespective of the configuration of the input data, the alignment proceeds in an optimal manner.

In the initial instance, the orientation of lidar data is facilitated by the alignment of lidargrams with photographs. The geocoding of the hybrid block is determined by the georeferencing of the images, which are the basis of the measurement of GCPs.

The second case is general in nature. That is to say, the external orientation elements of all images (photographs and lidargrams) are calculated in this instance, which in turn leads to a corrected external orientation of the point cloud.

The third case pertains to the alignment of images in the absence of GCPs, with the LiDAR cloud serving as the reference data.

In each of the three cases tested on the two test fields with different land-use and data characteristics, the results confirm that an accurate alignment of the data is possible despite the fact that the image matching was carried out with quality set on low level. The visual quality of the images was such that it was not possible to match them at a higher quality. This was due to the blurring of the images. It is evident that there is a necessity to enhance the quality of lidargram generation, which could result in a greater number of matches with higher precision. With regard to classical methods, it appears that the parameters and generation algorithm employed have attained their theoretical limits. It is anticipated that further research will be conducted with the utilisation of inpainting methodologies for the purpose of generating synthetic images.

To summarise, the preceding studies propose fresh opportunities for the combination of photogrammetric and scanning data by means of lidargrammetry. The findings substantiate the efficacy and legitimacy of the method.

Acknowledgements

We would like to express our gratitude to Prof. Krystian Pyka (AGH Kraków, Poland), Gottfried Mandlburger (TU Wien, Austria) and Dr Fabio Remondino (FBK Trento, Italy) for their valuable suggestions and creative discussions. In addition, the authentic data employed in the testing process was provided by Professor Gottfried Mandlburger of the Technical University of Vienna and Dr Fabio Remondino of the FBK Trento in Italy.

This research constitutes a component of the postdoctoral research project, which is receiving partial support from the "Inicjatywa Doskonałości - Uczelnia Badawcza" programme for the AGH University of Science and Technology (No. 4744). The project is under the direction of Antoni Rzonca.

References

Balntas, V., Johns, E., Tang, L., Mikolajczyk, K., 2016a. PN-Net: Conjoined Triple Deep Network for Learning Local Image Descriptors.

Balntas, V., Riba, E., Ponsa, D., Mikolajczyk, K., 2016b. Br. Mach. Vis. Conf. 2016, BMVC 2016 2016-Septe, 119.1-119.11.

Baltsavias, E.P., 1999. ISPRS J. Photogramm. Remote Sens. 54, 199–214.

Barroso Laguna, A., Riba, E., Ponsa, D., Mikolajczyk, K., 2019. Key.Net: Keypoint detection by handcrafted and learned CNN filters, in: Proceedings of the IEEE International Conference on Computer Vision. pp. 5835–5843.

Bobkowska, K., Inglot, A., Przyborski, M., Sieniakowski, J., Tysiąc, P., 2017. 10th Int. Conf. Environ. Eng. ICEE 2017 27–28.

Brun, A., Cucci, D.A., Skaloud, J., 2022. ISPRS J. Photogramm. Remote Sens. 189, 185–200.

cloudcompare.org, 2025. cloudcompare.org [WWW Document]. URL cloudcompare.org

Detone, D., Malisiewicz, T., Rabinovich, A., 2018. SuperPoint: Self-supervised interest point detection and description, in: IEEE Computer Society Conference on Computer Vision and Pattern Recognition Workshops. pp. 337–349.

Dreier, A., Janßen, J., Kuhlmann, H., Klingbeil, L., 2021. Remote Sens. 13.

Edstedt, J., Sun, Q., Bökman, G., Wadenbäck, M., Felsberg, M., 2023.

Elaksher, A., Ali, T., Alharthy, A., 2023. Remote Sens. 15.

Flood, M., Seube, N., Wagg, D., 2024. Photogramm. Eng. Remote Sensing 90, 69–74.

Fragkos, P., Ioannidis, C., 2016. Fourth Int. Conf. Remote Sens. Geoinf. Environ. 9688, 96881L.

Glira, P., Weidinger, C., Otepka-Schremmer, J., Ressl, C., Pfeifer, N., Haberler-Weber, M., 2023. Remote Sens. 15, 1–32.

Habib, A., Kersting, A.P., Bang, K.I., Lee, D.C., 2010. IEEE Trans. Geosci. Remote Sens. 48, 221–236.

Han, X., Leung, T., Jia, Y., Sukthankar, R., Berg, A.C., 2015. Proc. IEEE Comput. Soc. Conf. Comput. Vis. Pattern Recognit. 07-12-June, 3279–3286.

Han, X., Leung, T., Jia, Y., Sukthankar, R., Berg, A.C., 2024. DeDoDe: Detect, Don't Describe - Describe, Don't Detect for Local Feature Matching, in: Proceedings - 2024 International Conference on 3D Vision, 3DV 2024. pp. 148–157.

Harris, C., Stephens, M., 1988. A Combined Corner and Edge Detector, in: Proceedings of the Alvey Vision Conference. pp. 147–151.

https://colmap.github.io/, 2025. Colmap [WWW Document]. URL colmap.github.io%0A

Jayendra-Lakshman, M., Devarajan, V., 2013. ISPRS Ann. Photogramm. Remote Sens. Spat. Inf. Sci. 2, 157–162.

Kumar Mishra, R., 2012. Open Remote Sens. J. 5, 54–63.

Leica, 2024. Leica CityMapper 3 [WWW Document]. URL https://leica-geosystems.com/-/media/files/leicageosystems/products/datasheets/leica_citymapper_hybrid_sensor_ds.ashx?la=en (accessed 10.24.24).

Li, J., Hu, Q., Ai, M., 2020. IEEE Trans. Image Process. 29, 3296–3310.

Li, J., Yang, B., Chen, C., Habib, A., 2019. ISPRS J. Photogramm. Remote Sens. 158, 123–145.

Lohani, B., Ghosh, S., 2017. Proc. Natl. Acad. Sci. India Sect. A - Phys. Sci. 87, 567–579.

Lowe, D.G., 2004. Int. J. Comput. Vis. 60, 91–110.

Mandlburger, G., Wenzel, K., Spitzer, A., Haala, N., Glira, P., Pfeifer, N., 2017. ISPRS Ann. Photogramm. Remote Sens. Spat. Inf. Sci. 4, 259–266.

Mayr, A., Bremer, M., Rutzinger, M., 2020. ISPRS Ann. Photogramm. Remote Sens. Spat. Inf. Sci. 5, 765–772.

Mishchuk, A., Mishkin, D., Radenović, F., Matas, J., 2017. Adv. Neural Inf. Process. Syst. 2017-Decem, 4827–4838.

Morelli, L., Bellavia, F., Menna, F., Remondino, F., 2022. Photogrammetry Now and Then - From Hand-Crafted to Deep-Learning Tie Points, in: International Archives of the Photogrammetry, Remote Sensing and Spatial Information Sciences - ISPRS Archives. pp. 163–170.

Morelli, L., Ioli, F., Maiwald, F., Mazzacca, G., Menna, F., Remondino, F., 2024. Deep-image-matching: A toolbox for multiview image matching of complex scenarios, in: International Archives of the Photogrammetry, Remote Sensing and Spatial Information Sciences - ISPRS Archives. pp. 309–316.

Pentek, Q., Kennel, P., Allouis, T., Fiorio, C., Strauss, O., 2020. ISPRS J. Photogramm. Remote Sens. 166, 294–307.

Pfeifer, N., Mandlburger, G., Otepka, J., Karel, W., 2014. Comput. Environ. Urban Syst. 45, 125–136.

Pirotti, F., Piragnolo, M., Vettore, A., Guarnieri, A., 2022. Int. Arch. Photogramm. Remote Sens. Spat. Inf. Sci. - ISPRS Arch. 43, 353–359.

Ressl, C., Kager, H., Mandlburger, G., 2008. Iaprs Xxxvii 253–260.

Ressl, C., Mandlburger, G., Pfeifer, N., 2009. Laser scanning 2009, IAPRS XXXVIII, 195–200.

Riegl, 2024. Reigl VQ-1560 III-S [WWW Document]. URL http://riegl.com/nc/products/airborne-scanning/produktdetail/product/scanner/91/ (accessed 10.26.24).

RIEGL Laser Measurement Systems GmbH, 2022. RiProcess_Datasheet_2022-09-01.pdf.

Rodríguez-Cielos, R., Galán-García, J.L., Padilla-Domínguez, Y., Rodríguez-Cielos, P., Bello-Patricio, A.B., López-Medina, J.A., 2017. Appl. Sci. 7.

Rublee, E., Rabaud, V., Konolige, K., Bradski, G., 2011. Proc. IEEE Int. Conf. Comput. Vis. 2564–2571.

Rzonca, A., 2018. Meas. Autom. Monit. 64, 57–62.

Rzonca, A., Majek, K., 2016. Meas. Autom. Monit. 62, 268–273.

Sarlin, P.E., Detone, D., Malisiewicz, T., Rabinovich, A., 2020. SuperGlue: Learning Feature Matching with Graph Neural Networks, in: Proceedings of the IEEE Computer Society Conference on Computer Vision and Pattern Recognition. pp. 4937–4946.

Sun, J., Shen, Z., Wang, Y., Bao, H., Zhou, X., 2021. LoFTR: Detector-Free Local Feature Matching with Transformers, in: Proceedings of the IEEE Computer Society Conference on Computer Vision and Pattern Recognition. pp. 8918–8927.

Teo, T.A., Shih, T.Y., Lin, Y.T., Huang, C.M., 2010. 31st Asian Conf. Remote Sens. 2010, ACRS 2010 1, 459–464.

Terrasolid Ltd., 2022. 169–232.

Tian, Y., Fan, B., Wu, F., 2017. Proc. - 30th IEEE Conf. Comput. Vis. Pattern Recognition, CVPR 2017 2017-Janua, 6128–6136.

Toschi, I., Farella, E.M., Welponer, M., Remondino, F., 2021. ISPRS J. Photogramm. Remote Sens. 172, 160–170.

Tulldahl, H.M., Bissmarck, F., Larsson, H., Grönwall, C., Tolt, G., 2015. Electro-Optical Remote Sensing, Photonic Technol. Appl. IX 9649, 964903.

Vexcel, 2024. Vexcel Dragon 4.1 [WWW Document]. URL https://www.vexcel-imaging.com/ultracam-dragon-4-1/ (accessed 10.26.24).

www.agisoft.com, 2024.

Xianjia, Y., Salimpour, S., Queralta, J.P., Westerlund, T., 2022.

Yang, B., Chen, C., 2015. ISPRS J. Photogramm. Remote Sens. 101, 262–274.

Yoon, S.W., Park, S.Y., 2024. Stereo Vision SLAM with SuperPoint and SuperGlue, in: International Archives of the Photogrammetry, Remote Sensing and Spatial Information Sciences - ISPRS Archives. pp. 183–188.

Zahs, V., Winiwarter, L., Anders, K., Bremer, M., Rutzinger, M., Potučková, M., Höfle, B., 2022. Int. Arch. Photogramm. Remote Sens. Spat. Inf. Sci. - ISPRS Arch. 43, 1109–1116.

Zhang, X., Xiao, F., Zheng, M., Xie, Z., 2024. Eur. J. Remote Sens. 57.

Zhao, X., Wu, X., Chen, W., Chen, P.C.Y., Xu, Q., Li, Z., 2023a. IEEE Trans. Instrum. Meas. 72, 1–16.

Zhao, X., Wu, X., Miao, J., Chen, W., Chen, P.C.Y., Li, Z., 2023b. IEEE Trans. Multimed. 25, 3101–3112.

Zhu, B., Ye, Y., Zhou, L., Li, Z., Yin, G., 2021. ISPRS J. Photogramm. Remote Sens. 181, 129–147.